Designing (Ultra)Fine-Grained High-Entropy Alloys by Spark Plasma Sintering and Equal-Channel Angular Pressing

Lisa-Marie Rymer * , **Thomas Lindner** , **Philipp Frint** , **Martin Löbel** and **Thomas Lampke**

Institute of Materials Science and Engineering, Chemnitz University of Technology,
D-09107 Chemnitz, Germany; th.lindner@mb.tu-chemnitz.de (T.L.); philipp.frint@mb.tu-chemnitz.de (P.F.);
martin.loebel@mb.tu-chemnitz.de (M.L.); thomas.lampke@mb.tu-chemnitz.de (T.L.)
*** Correspondence: lisa-marie.rymer@mb.tu-chemnitz.de; Tel.: +49-371-531-37902

Abstract: Single-phase, face-centered cubic (FCC) high-entropy alloys (HEA) are promising materials for future applications. In order to improve the mechanical properties, especially the tensile strength of these materials, this study focuses on the combination of spark plasma sintering (SPS) and equal-channel angular pressing (ECAP). The initial fine-grained microstructure produced by SPS is further refined by ECAP in a 90°-die. Optical microscopy and electron backscatter diffraction (EBSD) confirm this considerable grain refinement, leads to a grain size below 1 μm after 1 ECAP pass. An alternating arrangement of fine-grained areas and much coarser regions, aligned under an angle of approximately 27°, is found. Moreover, a first microstructural investigation of the twin structure is conducted. The mechanical behavior was investigated by hardness measurements and tensile testing. Both the hardness and tensile strength are remarkably increased after ECAP. In contrast, the uniform elongation and elongation at fracture are significantly reduced due to the strengthening mechanisms of strain hardening and grain refinement. It is concluded that the combination of SPS and ECAP is an attractive approach for designing (ultra)fine-grained HEAs with superior properties. The investigated techniques could be applied to understand the underlying microstructural mechanisms.

Keywords: high-entropy alloy (HEA); equal-channel angular pressing (ECAP); spark plasma sintering (SPS); severe plastic deformation (SPD); microstructure; mechanical properties

1. Introduction

High-entropy alloys (HEA) gain an increasing scientific interest in the field of materials science due to their outstanding properties. The strength often exceeds comparable classical alloys with one property-determining main component. HEA are often described as multi-component alloys with at least five elements in equimolar ratio [1]. However, an entropy-based definition extends this definition of HEAs to materials with a high mixing configurational entropy resulting from the mixing of multiple elements in solid solution [2]. Therefore, alloys containing less than five elements, e.g., CrFeCoNi, are also referred to as HEAs. The microstructural and thermodynamic effects of high entropy, sluggish diffusion, large lattice distortion, and the cocktail effect [2] are responsible for their properties, e.g., a superior strength/ductility ratio. Microstructure adjustments offer a largely unexplored potential for further improvement. Severe plastic deformation (SPD) has already proven to be a suitable method to modify the density and structure of lattice defects in the microstructure of classical alloys. The corresponding deformation and strengthening mechanisms acting during SPD are well understood for pure metals and lots of conventional alloy systems such as aluminum

alloys. However, there is a limited knowledge on SPD of HEA, especially in terms of microstructural phenomena and the resulting mechanical properties.

To achieve an (ultra)fine-grained microstructure in HEAs, cold rolling [3–6], high pressure torsion (HPT) [7–13], and friction stir processing (FSP) [14–18] have been used so far. Since equal-channel angular pressing (ECAP) of high- and medium-entropy alloys requires special processing equipment such as suitable dies and machines, only a small number of scientific studies are dealing with HEAs [19–21]. A key advantage of ECAP compared to other SPD techniques is the combination of the following circumstances. ECAP provides a homogeneous simple shear deformation throughout the billet. Since the billet geometry does not change during processing [22,23], multiple passes of ECAP can be easily performed, enabling very large cumulative strains to be introduced into the material. Moreover, ECAP has excellent scale-up potential [24,25], which is the basis for technological applications in the future.

Since a microstructural analysis can be performed after each pass, ECAP is often used to study the evolution of deformation-induced microstructures. Typical microstructural features are high defect densities and low grain sizes, which significantly influence the material's strength [23,26]. In addition, the microstructure of severely plastically deformed high- and medium-entropy alloys is characterized by twin boundary structures, which also contribute to the refinement of the microstructure. Due to the chemical composition of HEAs in combination with plastic deformation, stacking faults and Lomer-Cottrell locks [7,8,12,13,21] may contribute to an enhancement of the mechanical properties.

Most of the scientific studies focus on HEAs produced by casting. As a result of a directional solidification during this production process, a coarse-grained microstructure characterized by aligned dendrites is generated. In order to guarantee quasi-isotropic mechanical properties, a subsequent recrystallization heat treatment of the cast microstructure is often required. In contrast, SPS provides a random fine-grained microstructure (depending on the powder fraction), which has isotropic mechanical properties. Preliminary work has shown that a combination of inert gas atomization and SPS produces dense compacts with a homogeneous distribution of the alloying elements [27]. It is reported that powder metallurgical processed HEAs have a higher strength but lower ductility than HEAs produced by casting [28]. The increased strength is derived from a pronounced grain boundary strengthening. The comparatively low ductility originates from a reduced free path for dislocation motion and a locally reduced cohesion due to microscopic voids or defects (e.g., pores and cracks).

The combination of SPS and ECAP, which has not been reported so far, is an attractive approach for the design of (ultra)fine-grained HEAs. This contributes to a detailed understanding of the strengthening mechanisms in HEAs induced by SPD.

2. Materials and Methods

The starting powder material was produced by inert gas atomization using Argon as protective gas to avoid impurities and oxidation products during the process. The particle size distribution was analyzed by laser diffraction analysis in a Cilas 920 (Cilas, Orléans, France) granulometer.

The nominal and the measured chemical compositions of the examined HEA powder is given in Table 1. This composition was determined in a preliminary work [29] using an energy-dispersive X-ray spectroscopy (EDS) system (EDAX, Mahwah, NJ, USA).

Table 1. Nominal and measured chemical composition in at.% of the atomized powder.

Material	Cr	Fe	Co	Ni
Nominal CrFeCoNi	25.0	25.0	25.0	25.0
Measured CrFeCoNi [29]	25.7	25.0	24.6	24.7

The atomized powder was processed into dense compacts by spark plasma sintering (SPS KCE FCT-HP D 25-SI, FCT Systeme GmbH, Frankenblick, Germany). The experimental setup consists of a die and a plunger both made of graphite. The inner diameter of the die was 40 mm. The sintering

temperature was set to 1050 °C, the heating rate to 100 K/min and the uniaxial sintering pressure to 50 MPa. The holding time was 13 min. A graphite foil was applied as a release agent between the die walls and the powder. Argon was used as process gas to avoid chemical reactions during the sintering process. Cooling of the samples was done unregulated within the SPS plant. A billet with a cross-section of 15×15 mm^2 and a length of approximately 37 mm was cut from the resulting semi-finished product (diameter 40 mm, height 16 mm).

A friction-optimized ECAP die with a channel angle of 90° and moving channel walls [25] was used for the severe plastic deformation. Therefore, a single ECAP pass resulted in an equivalent plastic strain of 1.15 [30]. The channel had a cross-section of 15×15 mm^2. ECAP was carried out with a pressing speed of 5 mm/min at room temperature. The utilized lubricant was Beruforge 150D (CARL BECHEM GMBH, Hagen, Germany), which is particularly suitable for severe plastic deformation [31]. The as-sintered and ECAP-processed materials were investigated with regard to their mechanical properties. The Vickers hardness (HV 10) was examined using an automatic hardness testing machine (KB 250 BVRZ, KB Prüftechnik GmbH, Hochdorf-Assenheim, Germany). The material's strength was determined by tensile testing. The machining of the tensile specimens from the ECAP-billet was carried out parallel to the z-plane (see Figure 1) using electrical discharge machining (EDM). The dog-bone shaped samples had a cross-section of 2.0×1.2 mm^2 and a gauge length of 5 mm. Quasi-static tensile tests (9 for each condition) at room temperature were performed using a standard tensile testing machine (ZwickRoell GmbH & Co. KG, Ulm, Germany) with an initial strain rate of $\dot{\varepsilon} = 10^{-3}$ s^{-1}. The corresponding strain was determined by digital image correlation (GOM Aramis, Germany).
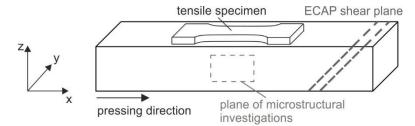

Figure 1. Schematic illustration of the equal-channel angular pressing (ECAP) billet. The pressing direction (parallel to the length axis of the die's exit channel), the plane of the microstructural investigations and the ECAP shear plane within the ECAP billet are marked.

For microstructural characterization, cross-sections of the as-sintered and ECAP-processed condition were prepared parallel to the y-plane (see Figure 1) using standardized metallographic preparation techniques. Finally, HCl and HNO$_3$-based etching was performed to visualize the grain boundaries. In order to receive an overview of the microstructure, examinations by optical microscopy (GX51 with a SC50 camera, both Olympus, Shinjuku, Japan) were performed. For a more detailed analysis of the microstructure, a field emission electron microscope NEON 40EsB (Zeiss, Jena, Germany) equipped with electron backscatter diffraction (EBSD) detector was used. The step size corresponded to 80 nm. The phases formed during the manufacturing process were qualitatively determined using X-ray diffraction (XRD) on a D8 Discover diffractometer (Bruker AXS, Billerica, MA, USA). This operates with Co Kα radiation, a voltage of 40 kV and a current of 40 mA. The diffraction angle 2θ included the range between 20° and 130°. The measurement using a 1D Lynxeye XE detector was carried out with a step size of 0.02° and 7 s/step.

3. Results and Discussion

3.1. Phase Composition and Particle Size Distribution

In order to verify the type of the lattice structure, a qualitative phase analysis of the as-sintered and ECAP-processed CrFeCoNi HEA was performed by means of XRD. The corresponding diffractogram

is shown in Figure 2a. A single-phase FCC lattice structure is formed, both in the as-sintered and ECAP-processed condition. It should be noted that the crystal structure of the multicomponent alloy differs from the constituent elements. The phase formation is in accordance with the feedstock powder characterized in a previous study [28]. Peak broadening is observed for the ECAP-processed material, which is most likely due to grain refinement and an increased defect density caused by SPD.
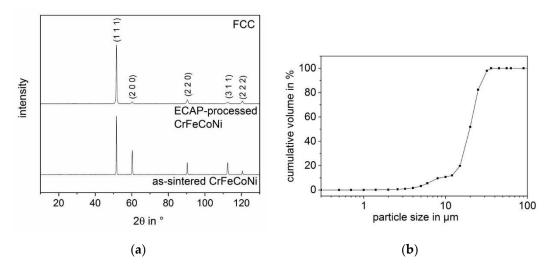

(**a**)　　　　　　　　　　　　　　　　　　　　　　　(**b**)

Figure 2. Results of diffractometry; (**a**) X-ray diffraction (XRD) diffractogram of the as-sintered and ECAP-processed materials, (**b**) cumulative particle size distribution of the atomized CrFeCoNi powder.

The resulting (cumulative) particle size distribution is shown in Figure 2b. It can be concluded that 98% of the particles are smaller than 32 μm.

3.2. Microstructural Characterization

Figure 3 shows optical microscopy images of the (a) as-sintered and (b) the ECAP-processed CrFeCoNi HEA. In the as-sintered condition, the former particle boundaries are still visible. The micrograph reveals a characteristic particle size, which corresponds to the results of the particle size distribution measurement shown in Figure 2b. The microstructure is also characterized by some micropores. In addition, the larger cavity in Figure 3a, marked with an orange circle, shows nearly the same shape and size as the powder particles, so it can be assumed that single powder particles broke off during the metallographic preparation. In the severely plastically deformed condition (see Figure 3b), the former particle boundaries are elongated and aligned under an angle of about 27° (to the pressing direction) as a consequence of simple shear during ECAP. Since optical microscopy is not suitable for a detailed microstructural characterization of fine-grained materials, EBSD investigations are necessary to clearly identify the grain size of the as-sintered and ECAP-processed material.

In Figure 4, the (a,e) image quality (IQ) maps, (b,f) orientation (OM) maps and (c,g) high angle grain boundary (HAGB) maps as well as the (d,h) grain size distribution for number and area fraction functions of the as-sintered (a–d) and the ECAP-processed (e–h) CrFeCoNi HEA are shown. The grain size was calculated according to DIN ISO 13067 and corresponds to the circle equivalent diameter [32]. Twin boundaries are considered when determining the grain size distribution. The as-sintered material exhibits some scratches (see Figure 4a) caused by the microstructural preparation. The OM in Figure 4b depicts equiaxed grains and many twin boundaries. Moreover, the microstructure is characterized by a random distribution of crystallographic orientations, which is typical for metals produced by sintering. The grain boundary map in Figure 4c reveals some grains with considerably larger diameter. This finding is also confirmed by the area fraction distribution in Figure 4d (blue line), which shows a characteristic peak at a grain size of 26 μm. However, the number fraction of this grain size only

amounts to 0.001 (red line). However, when considering the number fraction distribution (Figure 4d, red line), the majority of grains have a size below 10 µm.
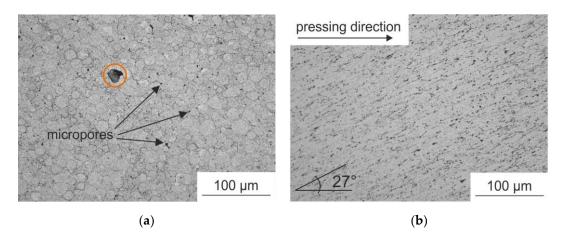

(**a**)   (**b**)

Figure 3. Optical microscopy images of etched (**a**) as-sintered and (**b**) ECAP-processed CrFeCoNi. In (**a**), some microspores are exemplary visible (marked with arrows). In the orange circle (**a**), a broken particle resulting from the metallographic preparation can be seen. After ECAP-processing, the former powder particles are elongated.
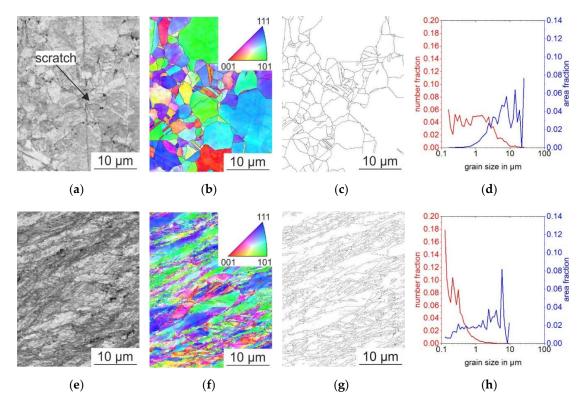

(**a**)   (**b**)   (**c**)   (**d**)

(**e**)   (**f**)   (**g**)   (**h**)

Figure 4. Results of electron backscatter diffraction (EBSD) measurements; (**a**,**e**) image quality (IQ) maps, (**b**,**f**) orientation (OM) maps and (**c**,**g**) high angle grain boundary (HAGB) maps as well as (**d**,**h**) grain size distributions for both number (red lines) and area fraction functions (blue lines) of the as-sintered (**a**–**d**) and the ECAP-processed (**e**–**h**) CrFeCoNi HEA. In (**g**), the microstructure appears very heterogeneously and regions with large as well as small sheared grains are identified. The area fraction distributions (blue lines) in (**d**,**h**) show peaks at grain sizes of 26 µm (as-sintered) and 6 µm (ECAP-processed) for the as-sintered and ECAP-processed material. Additionally, in (**d**,**h**) the number fraction distribution (red-lines) reveal a majority of grains with a size below 10 µm (as-sintered) and 1 µm (ECAP-processed).

In contrast, the material is sheared and pronounced grain refinement is observed after 1 ECAP pass (Figure 4e–h). The IQ map (see Figure 4e) shows an overall darker grey scale compared to the as-sintered condition. These local color differences indicate a heterogeneous distribution of inherent strain. The OM in Figure 4f verifies the presence of a considerable grain refinement caused by SPD. In addition, areas of varying distortions are found, which becomes even clearer when considering the grain boundary map in Figure 4g. This image reveals large regions with a low density of HAGBs. Regions with a high HAGB density exist next to areas characterized by a low density of HAGBs, which are typically aligned at an angle of approximately 27° (1 ECAP pass, 90° channel angle) [33]. It should be noted that the observed microstructure is heterogeneous, but does not show typical characteristics [34] of a deformation behavior that is predominantly controlled by shear banding. The area fraction distribution in Figure 4h (blue line) represents a peak at a grain size of 6 μm. The corresponding number fraction is only 0.0003 (Figure 4h, red line). It is assumed that areas having a low density of HAGBs originate from large grains of the as-sintered material. However, when considering the number fraction distribution (Figure 4h, red line), the predominant fraction of grains exhibits a size below 1 μm.

In addition, the EBSD measurements are also used to determine the twin structure. Figure 5 depicts the OMs of the (a) as-sintered and (b) ECAP-processed CrFeCoNi. Twins are marked by black arrows. The size of the twins in the as-sintered material strongly varies in the range of a few hundred nm and some μm. After ECAP-processing, a reduced thickness of twins is detected. Their size is about 100–300 nm. In addition, the misorientation angle distributions of the as-sintered and ECAP-processed material are displayed in Figure 5c,d.
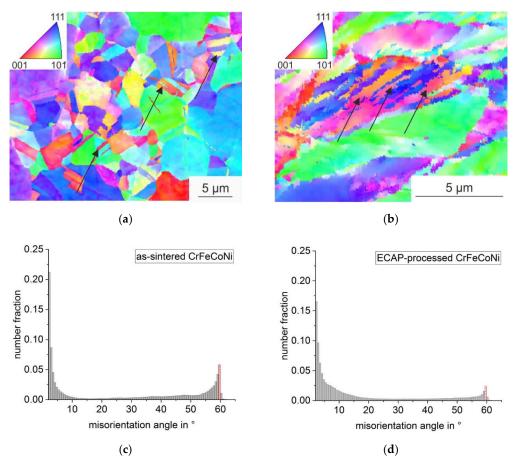

Figure 5. Results of EBSD measurements; orientation maps (OM) of the (**a**) as-sintered and (**b**) ECAP-processed CrFeCoNi as well as (**c**,**d**) the misorientation angle distribution. Twins are marked with black arrows in (**a**,**b**).

The number fraction of the as-sintered material shows especially low angle grain boundaries (LAGBs) up to a misorientation of 10° and HAGBs between 35° and 60°. According to ECAP, the misorientation angle distribution changes to a higher number fraction of LAGBs. The evolution of the misorientation angle is attributed to SPD. ECAP leads to the formation of deformation induced boundaries [35], which evolve into HAGBs during further straining. In addition, both diagrams show an increase of the number fraction at approximately 60°, most likely attributed to the presence of twins. The number fraction is decreased after SPD (see Figure 5c,d). It is assumed that on the one hand, the identification of very small deformation-induced twins via EBSD is limited due to the used step size during the measurement. On the other hand, the strong increase of deformation-induced LAGBs (caused by dislocation multiplication) leads to a superposition of a relatively low fraction of twin-related misorientations. This is in contrast to a study of an austenitic stainless steel by Zhang et al. [36], which observed a remarkable increase of the twin density after 1 ECAP pass using a die with a channel angle of 90°. The dominant deformation mechanism in the investigated CrFeCoNi during ECAP-processing is assumed to be dislocation slip. However, a comprehensive study of twinning in sintered CrFeCoNi during ECAP is needed for a profound scientific understanding of the underlying microstructural and micromechanical mechanisms.

3.3. Mechanical Characterization

For a characterization of the deformation behavior, Vickers hardness measurement (HV 10) as well as tensile tests were conducted. The Vickers indenter was placed on the investigation plane for microstructural characterizations (y-plane, see Figure 1). The results of the hardness measurements are shown in Figure 6a. The scatter bars mark the minimum and maximum hardness values. When comparing the as-sintered (192 HV) and the ECAP-processed (420 HV) condition of the CrFeCoNi HEA, a significant hardness improvement of approximately 120% was observed after ECAP.
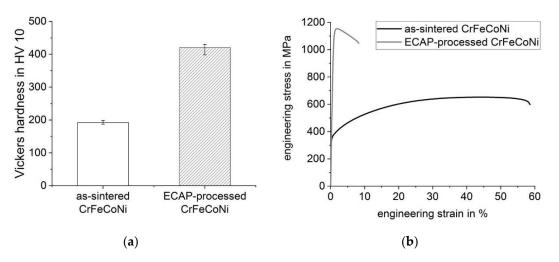

Figure 6. Results of mechanical testing; (**a**) Vickers hardness HV 10 and (**b**) engineering stress–strain-curves of the as-sintered and ECAP-processed CrFeCoNi.

Figure 6b shows representative tensile curves of the as-sintered and ECAP-processed CrFeCoNi HEA. The mean values of the results of mechanical testing are summarized in Table 2. Compared to a cast alloy of the same composition, investigated in the literature [37], the powder metallurgical condition of the present study shows significantly different mechanical properties. For instance, the yield strength (YS) of the as-sintered HEA is 355 MPa, which is 150% higher than that of the cast alloy (140 MPa [37]). The CrFeCoNi alloy in the as-solidified state used for the comparison had a grain length of 200–300 μm and a grain width of 100–150 μm [37]. It should be noted that the present as-sintered alloy has a grain size of less than 26 μm and therefore a direct comparison is not possible. However, this does not alter the statement that a significant increase in strength can be achieved

simply by changing the manufacturing process. After 1 ECAP pass, a further significant increase in yield strength and ultimate tensile strength (UTS) is found. The YS is increased by a factor of 3 to more than 1 GPa. However, a simultaneous decrease in uniform elongation (UE) and elongation at failure (EF) is visible. A comparison of both curves in Figure 6b also reveals a fundamentally different strain hardening behavior of the investigated material conditions. For a comprehensible discussion of this difference, the ratio of YS-to-UTS is helpful. This ratio is 0.54 in the as-sintered condition, which indicates a pronounced strain hardening. In contrast, the ECAP-deformed HEA shows almost no strain hardening since the ratio is 0.91. Additionally, a different magnitude of softening beyond the UTS is apparent. For the as-sintered material, only slight softening is found, while the deformation behavior of the ECAP-processed HEA is characterized by a pronounced decrease of the stress until fracture.

Table 2. Mechanical properties of the as-sintered and ECAP-processed CrFeCoNi.

Material	YS in MPa	UTS in MPa	UE in %	EF in %
As-sintered CrFeCoNi	355	654	44	60
ECAP-processed CrFeCoNi	1032	1136	~1	7

It is well known that severe plastic deformation leads to dislocation multiplication and grain refinement, which leads to a significant increase in hardness and strength in most metallic material [38]. An increased dislocation density causes more pronounced dislocation–dislocation interactions, thus impeding their motion [38–40]. Moreover, the storage capacity for further deformation-induced dislocations decreases since dislocation annihilation becomes more distinctive, particularly in FCC-materials such as the investigated HEA. This phenomenon is responsible for a reduced ductility of the ECAP-deformed HEA of the present study.

These results show that the combination of powder metallurgical processing and ECAP of CrFeCoNi leads to an extraordinary strength increase from 140 MPa (cast condition [37]) to more than 1 GPa and therefore highlight the feasibility of this procedure for (ultra)fine-grained high-strength HEAs.

4. Conclusions

The present study deals with the combination of spark plasma sintering and equal-channel angular pressing (90° channel angle) to produce an (ultra)fine-grained high-entropy alloy (CrFeCoNi). The resulting mechanical behavior and the microstructural evolution were investigated. The following conclusions can be drawn:

(1) XRD measurements reveal an FCC structure before and after ECAP-processing of sintered CrFeCoNi, showing that the single-phase state was retained. However, the peaks of the ECAP-processed material are broadened, which is typical after ECAP-processing.

(2) Microstructural investigations (by optical microscopy and EBSD) confirm a considerable grain refinement. ECAP-processing leads to a majority of grains with a size below 1 μm. The corresponding microstructure is characterized by elongated grains due to the induced simple shear deformation. Differently distorted areas are found. Fine-grained areas alternate with areas characterized by much coarser grains. Both areas are arranged under an angle of approximately 27° (to the pressing direction). The thickness of the large twins (up to several μm) in the as-sintered material was reduced by ECAP to approximately 100–300 nm. From the present study, it is assumed that the dominating deformation mechanism in the investigated CrFeCoNi HEA during ECAP-processing is dislocation slip.

(3) The mechanical properties (hardness and tensile properties) are significantly increased due to the introduction of defects and the formation of HAGBs during ECAP. Compared to a cast condition of the same alloy, the sintered condition shows significantly different mechanical properties. For instance, the YS of the as-sintered HEA is 150% higher than that of a cast counterpart (reported in the literature). A further significant increase of YS and UTS is found after a single pass

of ECAP. The YS is increased to more than 1 GPa. A comparison of both conditions (as-sintered, ECAP-deformed) reveals a fundamentally different strain hardening behavior of CrFeCoNi, which is discussed in detail.

These results demonstrate that the combination of SPS and ECAP of CrFeCoNi leads to an extraordinary high strength of more than 1 GPa, which highlights its excellent potential for producing (ultra)fine-grained high-strength HEAs.

References

1. Yeh, J.W.; Chen, S.K.; Lin, S.J.; Gan, J.Y.; Chin, T.S.; Shun, T.T.; Tsau, C.H.; Chang, S.Y. Nanostructured high-entropy alloys with multiple principal elements: Novel alloy design concepts and outcomes. *Adv. Eng. Mater.* **2004**, *6*, 299–303. [CrossRef]

2. Miracle, D.B.; Senkov, O.N. A critical review of high entropy alloys and related concepts. *Acta Mater.* **2017**, *122*, 448–511. [CrossRef]

3. Gwalani, B.; Soni, V.; Lee, M.; Mantri, S.A.; Ren, Y.; Banerjee, R. Optimizing the coupled effects of Hall-Petch and precipitation strengthening in a $Al_{0.3}CoCrFeNi$ high entropy alloy. *Mater. Des.* **2017**, *121*, 254–260. [CrossRef]

4. Gwalani, B.; Gorsse, S.; Choudhuri, D.; Zheng, Y.; Mishra, R.S.; Banerjee, R. Tensile yield strength of a single bulk $Al_{0.3}CoCrFeNi$ high entropy alloy can be tuned from 160 MPa to 1800 MPa. *Scr. Mater.* **2019**, *162*, 18–23. [CrossRef]

5. Liu, K.; Komarasamy, M.; Gwalani, B.; Shukla, S.; Mishra, R.S. Fatigue behavior of ultrafine grained triplex $Al_{0.3}CoCrFeNi$ high entropy alloy. *Scr. Mater.* **2019**, *158*, 116–120. [CrossRef]

6. Shukla, S.; Mishra, R.S. Excellent high cycle fatigue properties of a novel ultrafine-grained medium entropy alloy. *Mater. Sci. Eng. A* **2020**, *779*, 139122. [CrossRef]

7. Gubicza, J.; Hung, P.T.; Kawasaki, M.; Han, J.K.; Zhao, Y.; Xue, Y.; Lábár, J.L. Influence of severe plastic deformation on the microstructure and hardness of a CoCrFeNi high-entropy alloy: A comparison with CoCrFeNiMn. *Mater. Charact.* **2019**, *154*, 304–314. [CrossRef]

8. Heczel, A.; Kawasaki, M.; Lábár, J.L.; Jang, J.-I.; Langdon, T.G.; Gubicza, J. Defect structure and hardness in nanocrystalline CoCrFeMnNi High-Entropy Alloy processed by High-Pressure Torsion. *J. Alloys Compd.* **2017**, *711*, 143–154. [CrossRef]

9. Lee, D.H.; Choi, I.C.; Seok, M.Y.; He, J.; Lu, Z.; Suh, J.Y.; Kawasaki, M.; Langdon, T.G.; Jang, J.I. Nanomechanical behavior and structural stability of a nanocrystalline CoCrFeNiMn high-entropy alloy processed by high-pressure torsion. *J. Mater. Res.* **2015**, *30*, 2804–2815. [CrossRef]

10. Schuh, B.; Mendez-Martin, F.; Völker, B.; George, E.P.; Clemens, H.; Pippan, R.; Hohenwarter, A. Mechanical properties, microstructure and thermal stability of a nanocrystalline CoCrFeMnNi high-entropy alloy after severe plastic deformation. *Acta Mater.* **2015**, *96*, 258–268. [CrossRef]

11. Schuh, B.; Pippan, R.; Hohenwarter, A. Tailoring bimodal grain size structures in nanocrystalline compositionally complex alloys to improve ductility. *Mater. Sci. Eng. A* **2019**, *748*, 379–385. [CrossRef]

12. Skrotzki, W.; Pukenas, A.; Joni, B.; Odor, E.; Ungar, T.; Hohenwarter, A.; Pippan, R.; George, E.P. Microstructure and texture evolution during severe plastic deformation of CrMnFeCoNi high-entropy alloy. *IOP Conf. Ser. Mater. Sci. Eng.* **2017**, *194*, 012028. [CrossRef]

13. Wu, W.; Song, M.; Ni, S.; Wang, J.; Liu, Y.; Liu, B.; Liao, X. Dual mechanisms of grain refinement in a FeCoCrNi highentropy alloy processed by highpressure torsion. *Sci. Rep.* **2017**, *7*, 46720. [CrossRef] [PubMed]

14. Kumar, N.; Komarasamy, M.; Nelaturu, P.; Tang, Z.; Liaw, P.K.; Mishra, R.S. Friction stir processing of a high entropy alloy $Al_{0.1}CoCrFeNi$. *JOM* **2015**, *67*, 1007–1013. [CrossRef]

15. Komarasamy, M.; Kumar, N.; Tang, Z.; Mishra, R.S.; Liaw, P.K. Effect of microstructure on the deformation mechanism of friction stir-processed $Al_{0.1}CoCrFeNi$ high entropy alloy. *Mater. Res. Lett.* **2014**, *3*, 30–34. [CrossRef]

16. Nene, S.S.; Liu, K.; Frank, M.; Mishra, R.S.; Brennan, R.E.; Cho, K.C.; Li, Z.; Raabe, D. Enhanced strength and ductility in a friction stir processing engineered dual phase high entropy alloy. *Sci. Rep.* **2017**, *7*, 16167. [CrossRef]

17. Nene, S.S.; Frank, M.; Liu, K.; Mishra, R.S.; McWilliams, B.A.; Cho, K.C. Extremely high strength and work hardening ability in a metastable high entropy alloy. *Sci. Rep.* **2018**, *8*, 9920. [CrossRef]

18. Liu, K.; Nene, S.S.; Frank, M.; Sinha, S.; Mishra, R.S. Metastability-assisted fatigue behavior in a friction stir processed dual-phase high entropy alloy. *Mater. Res. Lett.* **2018**, *6*, 613–619. [CrossRef]

19. Hammond, V.H.; Atwater, M.A.; Darling, K.A.; Nguyen, H.Q.; Kecskes, L.J. Equal-Channel Angular Extrusion of a Low-Density High-Entropy Alloy Produced by High-Energy Cryogenic Mechanical Alloying. *JOM* **2014**, *66*, 2021–2029. [CrossRef]

20. Shahmir, H.; Mousavi, T.; He, J.; Lu, Z.; Kawasaki, M.; Langdon, T.G. Microstructure and properties of a CoCrFeNiMn high-entropy alloy processed by equal-channel angular pressing. *Mater. Sci. Eng. A* **2017**, *705*, 411–419. [CrossRef]

21. Deng, H.W.; Xie, Z.M.; Zhao, B.L.; Wang, Y.K.; Wang, M.M.; Yang, J.F.; Zhang, T.; Xiong, Y.; Wang, X.P.; Fang, Q.F. Tailoring mechanical properties of a CoCrNi medium-entropy alloy by controlling nanotwin-HCP lamellae and annealing twins. *Mater. Sci. Eng. A* **2019**, *744*, 241–246. [CrossRef]

22. Segal, V.M. Materials processing by simple shear. *Mater. Sci. Eng. A* **1995**, *197*, 157–164. [CrossRef]

23. Valiev, R.Z.; Langdon, T.G. Principles of equal-channel angular pressing as a processing tool for grain refinement. *Prog. Mater. Sci.* **2006**, *51*, 881–981. [CrossRef]

24. Frint, P.; Hockauf, M.; Halle, T.; Strehl, G.; Lampke, T.; Wagner, M.F.X. Microstructural features and mechanical properties after industrial scale ECAP of an Al-6060 alloy. *Mater. Sci. Forum* **2011**, *667–669*, 1153–1158. [CrossRef]

25. Frint, S.; Hockauf, M.; Frint, P.; Wagner, M.F.X. Scaling up Segal's principle of Equal-Channel Angular Pressing. *Mater. Des.* **2016**, *97*, 502–511. [CrossRef]

26. Furukawa, M.; Horita, Z.; Langdon, T.G. Developing ultrafine grain sizes using severe plastic deformation. *Adv. Eng. Mater.* **2001**, *3*, 121–125. [CrossRef]

27. Löbel, M.; Lindner, T.; Pippig, R.; Lampke, T. High-temperature wear behaviour of spark plasma sintered $AlCoCrFeNiTi_{0.5}$ high-entropy alloy. *Entropy* **2019**, *21*, 582. [CrossRef] [PubMed]

28. Torralba, J.M.; Alvaredo, P.; García-Junceda, A. High-entropy alloys fabricated via powder metallurgy. A critical review. *Powder Metall.* **2019**, *62*, 84–114. [CrossRef]

29. Löbel, M.; Lindner, T.; Hunger, R.; Berger, R.; Lampke, T. Precipitation hardening of the HVOF sprayed single-phase high-entropy alloy CrFeCoNi. *Coatings* **2020**, *10*, 701. [CrossRef]

30. Iwahashi, Y.; Wang, J.; Horita, Z.; Nemoto, M.; Langdon, T.G. Principle of equal-channel angular pressing for the processing of ultra-fine grained materials. *Scr. Mater.* **1996**, *35*, 143–146. [CrossRef]

31. Frint, P.; Wagner, M.F.X.; Weber, S.; Seipp, S.; Frint, S.; Lampke, T. An experimental study on optimum lubrication for large-scale severe plastic deformation of aluminum-based alloys. *J. Mater. Process. Technol.* **2017**, *239*, 222–229. [CrossRef]

32. DIN ISO 13067:2015-12. *Microbeam Analysis—Electron Backscatter Diffraction—Measurement of Average Grain Size*; Beuth Verlag GmbH: Berlin, Germany, 2015.

33. Beyerlein, I.J.; Tomé, C.N. Analytical modeling of material flow in equal channel angular extrusion (ECAE). *Mater. Sci. Eng. A* **2004**, *380*, 171–190. [CrossRef]

34. Frint, P.; Wagner, M.F.X. Strain partitioning by recurrent shear localization during equal-channel angular pressing of an AA6060 aluminum alloy. *Acta Mater.* **2019**, *176*, 306–317. [CrossRef]

35. Zolotorevsky, N.Y.; Rybin, V.V.; Matvienko, A.N.; Ushanova, E.A.; Philippov, S.A. Misorientation angle distribution of deformation-induced boundaries provided by their EBSD-based separation from original grain boundaries: Case study of copper deformed by compression. *Mater. Charact.* **2019**, *147*, 184–192. [CrossRef]

36. Zhang, J.; Han, W.; Rui, W.; Li, J.; Huang, Z.; Sui, F. Deformation Mechanisms of 316L Austenitic Stainless Steel Tubes under Equal Channel Angular Pressing. *J. Mater. Eng. Perform.* **2020**, *29*, 1253–1261. [CrossRef]

37. Salishchev, G.A.; Tikhonovsky, M.A.; Shaysultanov, D.G.; Stepanov, N.D.; Kuznetsov, A.V.; Kolodiy, I.V.; Tortika, A.S.; Senkov, O.N. Effect of Mn and v on structure and mechanical properties of high-entropy alloys based on CoCrFeNi system. *J. Alloys Compd.* **2014**, *591*, 11–21. [CrossRef]

38. Segal, V. Review: Modes and processes of severe plastic deformation (SPD). *Materials* **2018**, *11*, 1175. [CrossRef]

39. Pande, C.S.; Cooper, K.P. Nanomechanics of Hall-Petch relationship in nanocrystalline materials. *Prog. Mater. Sci.* **2009**, *54*, 689–706. [CrossRef]

40. Schneider, M.; George, E.P.; Manescau, T.J.; Záležák, T.; Hunfeld, J.; Dlouhý, A.; Eggeler, G.; Laplanche, G. Analysis of strengthening due to grain boundaries and annealing twin boundaries in the CrCoNi medium-entropy alloy. *Int. J. Plast.* **2020**, *124*, 155–169. [CrossRef]

Publisher's Note: MDPI stays neutral with regard to jurisdictional claims in published maps and institutional affiliations.